NUMERICAL MODELING OF SUPERCAVITATING AND SURFACE-PIERCING PROPELLER FLOWS

Yin Lu Young and Spyros A. Kinnas

The University of Texas at Austin, Austin, TX 78712, USA

A 3-D panel method has been extended to model the flow around fully submerged supercavitating propellers and surface-piercing propellers. Overviews of the formulation and solution methodology is presented. Comparisons of the numerical predictions with measurements from experiments are given. Discussion of the numerical results, and initial work on modeling of impact flows are provided.

1 Introduction

Supercavitating propellers are often considered as the most fuel efficient propulsive device for high speed vessels. They are characterized by blade sections with thick trailing edges. The resulting supercavities tend to have smaller volume change and produce bubbles that collapse downstream of the blade trailing edge, which result in reduced noise and blade surface erosion.

A surface-piercing, or partially submerged, propeller is a special type of supercavitating propeller which operates at partially submerged conditions. A surface-piercing propeller can be more efficient than an submerged propeller because: 1) reduction of appendage drag due to shafts, struts, propeller hub, etc.; 2) larger propellers since their size is not limited by the blade tip clearance from the hull or the maximum vessel draft; and 3) reduction of blade surface erosion caused by the growing and collapsing of cavities.

In the past, the design of surface-piercing propellers involved trial-and-error procedure using the measured performance of test models in free-surface tunnels or towing tanks. However, most of the trial-and-error approaches do not provide information about the dynamic blade loads nor the average propeller forces (Olofsson (1996)). Model tests are also hampered by scaling effects (Shen (1975) and Scherer (1977)) and influences of test techniques (Morgan (1966), Suhrbier and Lecoffre (1986)). Numerical methods, on the other hand, were not able to model the real phenomena. Difficulties in modeling surface-piercing propellers include: 1) insufficient understanding of the physical phenomena at the blade's entry to, and exit from, the free surface; 2) the modeling of very thick and very long ventilated cavities, which are also interrupted by the free surface; and 3) the modeling of water jets and change in free surface elevation, as well as blade vibrations, associated with the blade's entry to, and exit from, the free surface.

The objective of this research is to extend a three-dimensional (3-D) boundary element (panel) method to predict the performance of supercavitating and surface-piercing propellers.

The first effort to model surface-piercing propeller was carried out by Oberembt (1968). He used a lifting line approach along with the assumption that the propeller is lightly loaded such that no natural ventilation of the propeller and its vortex wake occur. A lifting-line approach which included the effect of propeller ventilation was introduced by Furuya (1984).

A 3-D lifting surface vortex-lattice method for the analysis of super-cavitating propellers have been developed by Kudo and Ukon (1994) and Kudo and Kinnas (1995). The method is capable of analyzing separated flows behind thick trailing edge blade sections under fully wetted, partially cavitating, or supercavitating flow conditions. However, for surface-piercing propellers, the lifting surface method performs all the calculations assuming the propeller is fully submerged, and then it multiplies the resulting forces by the propeller submergence ratio. As a result, only the mean forces can be predicted as the complicated phenomena of blades' entry to, and exit from, the water surface are completely ignored.

A 2-D time-marching panel method was developed by Savineau and Kinnas (1995) for the analysis of the flow field around a fully ventilated surface-piercing hydrofoil. However, this method only accounts for the hydrofoil's entry to, but not exit from, the water surface.

The presented technique, PROPCAV, is a low-order potential-based panel method. It models propeller sheet cavitation in the framework of a boundary-value problem: for a given cavitation number and inflow, the position of the cavity surface is determined in an iterative manner until both a prescribed pressure condition and a zero normal velocity condition are satisfied on the cavity surface. The method was first developed by Kinnas and Fine (1991) for the nonlinear analysis of flow around partially and supercavitating 2-D hydrofoils. It was then extended to treat partially cavitating 3-D hydrofoils (Kinnas and Fine (1993)) and cavitating propellers subjected to non-axisymmetric inflows (Fine (1992), Kinnas and Fine (1992)). Recently, PROPCAV has been extended to predict leading edge and mid-chord partial cavitation on either the face or the back of the blades by Mueller (1998) and Mueller and Kinnas (1999). In Young and Kinnas (2001), PROPCAV was further extended to predict the occurrence of general cavity planforms - including partial cavitation, supercavitation, and mixed partial/supercavitation on both the face and the back of the blades with searched cavity detachment. In this work, the method is further extended to predict the performance of supercavitating and surface-piercing propellers. An overview of the formulation is presented first. Comparisons of the numerical predictions with experimental data are given. In addition, initial work on the modeling of the flow at the instant of impact is provided.

2 Formulation

2.1 Fully Submerged Propellers

This section summarizes the formulation of the cavitating flow around a fully submerged propeller given by Fine (1992) and Young and Kinnas (2001).

Consider a cavitating propeller subject to a general inflow wake, $\vec{q}_{wake}(x_s, y_s, z_s)$, as shown in Figure 1. The inflow wake is expressed in terms of the absolute (ship fixed) system of cylindrical coordinates (x_s, y_s, z_s). The inflow velocity, $\vec{q}_{in}$, with respect to the propeller fixed coordinates (x, y, z), can be expressed as the sum of the inflow wake velocity, $\vec{q}_{wake}$, and the propeller's angular velocity $\vec{\omega}$, at a given location $\vec{x}$:

$$\vec{q}_{in}(x, y, z, t) = \vec{q}_{wake}(x, r, \theta_B - \omega t) + \vec{\omega} \times \vec{x} \tag{1}$$

where $r = \sqrt{y^2 + z^2}$, $\theta_B = \arctan(z/y)$ and $\vec{x} = (x, y, z)$.

The inflow, $\vec{q}_{wake}$, is assumed to be the *effective wake*, i.e. it includes the interaction between the vorticity in the inflow and the propeller (Choi (2000), Kinnas et al. (2000)). The resulting flow is assumed to be incompressible and inviscid. The total velocity field, $\vec{q}$, can be expressed in terms of $\vec{q}_{in}$ and the perturbation potential, ϕ, as follows:

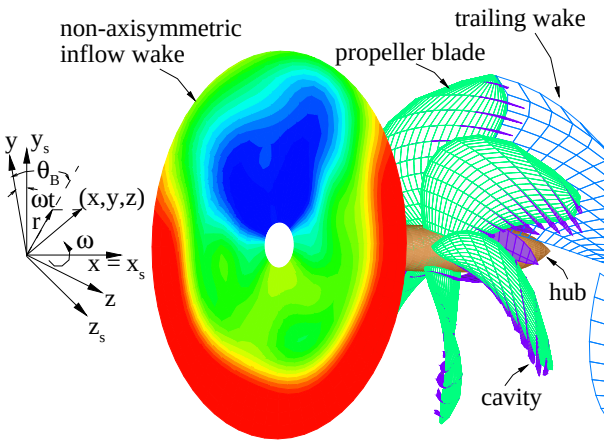

Figure 1: Propeller subjected to a general inflow wake. The propeller fixed (x, y, z) and ship fixed (x_s, y_s, z_s) coordinate systems are also shown.

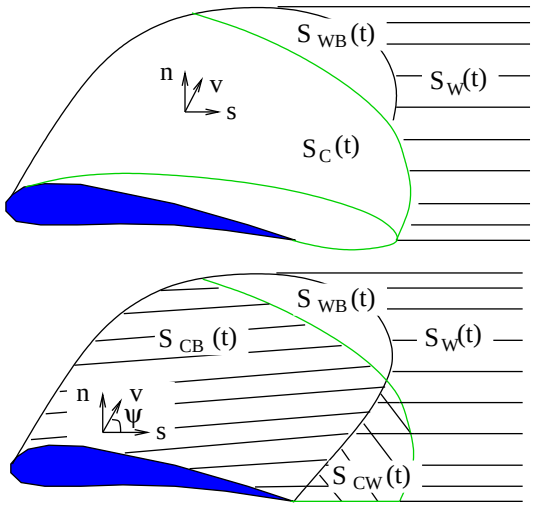

Figure 2: Top: Definition of the exact surface. Bottom: Definition of the approximated cavity surface.

$$\vec{q}(x,y,z,t) = \vec{q}_{in}(x,y,z,t) + \nabla\phi(x,y,z,t) \tag{2}$$

where ϕ satisfies the Laplace's equation in the fluid domain (i.e. $\nabla^2\phi = 0$). The potential, ϕ, at every point p on the combined wetted blade and cavity surface, $S_{WB}(t) \cup S_C(t)$, must satisfy Green's third identity:

$$2\pi\phi_p(t) = \int\int_{S_{WB}(t)\cup S_C(t)} \left[\phi_q(t)\frac{\partial G(p;q)}{\partial n_q(t)} - G(p;q)\frac{\partial \phi_q(t)}{\partial n_q(t)}\right] dS + \int\int_{S_W(t)} \Delta\phi(r_q,\theta_q,t)\frac{\partial G(p;q)}{\partial n_q(t)} dS \tag{3}$$

where the subscript q corresponds to the variable point in the integration. $G(p;q) = 1/R(p;q)$ is the Green's function with $R(p;q)$ being the distance between points p and q. $\vec{n}_q$ is the unit vector normal to the integration surface, pointing into the fluid domain. $\Delta\phi$ is the potential jump across the wake surface, $S_W(t)$. The definitions of S_{WB}, S_C and S_W are depicted in Figure 2.

Equation 3 should be applied on the "exact" cavity surface S_C, as shown in the drawing at the top of Figure 2. However, the cavity surface is not known and has to be determined as part of the solution. In this work, an approximated cavity surface, shown in the drawing at the bottom of Figure 2, is used. The approximated cavity surface is comprised of the blade surface underneath the cavity, S_{CB}, and the portion of the wake surface which is overlapped by the cavity, S_{CW}. The justification for making this approximation, as well as a measure of its effect on the cavity solution can be found in Kinnas and Fine (1993) and Fine (1992).

Using the approximated cavity surface, Eqn. 3 is then decomposed into a summation of integrals over the blade surface, S_B ($\equiv S_{CB} + S_{WB}$), and the portion of the wake surface which is overlapped by the cavity, S_{CW} (Young and Kinnas (2001)).

2.1.1 Kinematic Boundary Condition on Wetted Part of the Blade

The kinematic boundary condition requires the flow to be tangent to the wetted blade surface. Thus, the source strengths, $\frac{\partial\phi}{\partial n}$, are known in terms of the inflow velocity, $\vec{q}_{in}$:

$$\frac{\partial\phi(x,y,z,t)}{\partial n} = -\vec{q}_{in}(x,y,z,t)\cdot\vec{n} \tag{4}$$

2.1.2 Dynamic Boundary Condition on Cavitating Surfaces

The dynamic boundary condition on the cavitating blade and wake surfaces requires the pressure everywhere on the cavity to be constant and equal to the vapor pressure, P_v. By applying Bernoulli's equation, the total velocity on the cavity, $\vec{q}_c$, can be expressed as follows:

$$\vec{q}_c{}^2 = n^2D^2\sigma_n + |\vec{q}_{wake}|^2 + \omega^2r^2 - 2gy_s - 2\frac{\partial\phi}{\partial t} \tag{5}$$

where $\sigma_n \equiv (P_o - P_v)/(\frac{\rho}{2}n^2D^2)$ is the cavitation number; ρ is the fluid density and r is the distance from the axis of rotation. P_o is the pressure far upstream on the shaft axis; g is the acceleration of gravity and y_s is the ship fixed coordinate, shown in Figure 1. $n = \omega/2\pi$ and D are the propeller rotational frequency and diameter, respectively.

On the cavitating blade surface, the known values of ϕ can be obtained from the integration of $\frac{\partial\phi}{\partial s}$, which is expressed as follows (Fine (1992)):

$$\frac{\partial\phi}{\partial s} = -\vec{q}_{in}\cdot\vec{s} + V_v\cos\psi + \sin\psi\sqrt{|\vec{q}_c|^2 - V_v^2} \tag{6}$$

where $V_v \equiv \frac{\partial\phi}{\partial v} + \vec{q}_{in}\cdot\vec{v}$, and ψ is the angle between s and v directions (as defined in Figure 2).

On the cavitating wake surface, the coordinate $\vec{s}$ is assumed to follow the streamline [1]. Thus, the following expression can be derived for $\frac{\partial\phi}{\partial s}$:

$$\frac{\partial\phi}{\partial s} = -\vec{q}_{in}\cdot\vec{s} + |\vec{q}_c| \tag{7}$$

[1] Fine (1992) found that the effect of the cross-flow term in the cavitating wake region has very little effect on the solution.

2.1.3 Kinematic Boundary Condition on Cavitating Surfaces

The kinematic boundary condition on the cavity requires the total velocity normal to the cavity to be zero, which renders the following equation for the cavity thickness (h) on the blade (Fine (1992)):

$$\frac{\partial h}{\partial s}\left[V_s - \cos\psi V_v\right] + \frac{\partial h}{\partial v}\left[V_v - \cos\psi V_s\right] = \sin^2\psi\left(V_n - \frac{\partial h}{\partial t}\right) \tag{8}$$

where $V_s \equiv \frac{\partial\phi}{\partial s} + \vec{q}_{in}\cdot\vec{s}$ and $V_n \equiv \frac{\partial\phi}{\partial n} + \vec{q}_{in}\cdot\vec{n}$.

Assuming again that the span-wise cross-flow velocity on the wake surface is small, the kinematic boundary condition reduces to the following expression for the cavity thickness (h_w) on the wake (Fine (1992)):

$$\left[\frac{\partial\phi^+}{\partial n}(t) - \frac{\partial\phi^-}{\partial n}(t)\right] - \frac{\partial h_w}{\partial t} = |\vec{q_c}|\frac{\partial h_w}{\partial s} \tag{9}$$

It should be noted that h and h_w are defined normal to the blade and wake surfaces, respectively.

2.1.4 Kutta Condition

The Kutta condition requires that the velocity at the propeller trailing edge to be finite, i.e. $\nabla\phi < \infty$.

2.1.5 Cavity Closure Condition

The cavity closure condition requires that the cavity height at the trailing edge of the cavity to be zero.

2.1.6 Solution Method

The unsteady cavity problem is solved by inverting Eqn. 3 subjected to conditions 4, 6, 7, as well as the Kutta and cavity closure conditions. The numerical implementation is described in detail in Fine (1992), Kinnas and Fine (1992), and Young and Kinnas (2001). In brief, for a given cavity planform, Green's formula is solved with respect to the unknown ϕ on the wetted blade surface and the unknown $\frac{\partial\phi}{\partial n}$ on the cavity surface. The cavity heights are then determined by integrating Eqns. 8 and 9. The correct cavity planform is obtained in an iterative manner by satisfying the cavity closure condition. The split-panel technique developed by Fine (1992) and Kinnas and Fine (1992) is used to treat blade and wake panels that are intersected by the cavity trailing edge.

2.2 Partially Submerged Propellers

The formulation for partially submerged propellers is the same as that for fully submerged propellers with the following exceptions:

- The dynamic boundary condition requires that the pressure everywhere on the free surface and on the ventilated cavity surface to be constant and equal to the *atmospheric* pressure, p_{atm}.

- A linearized free surface condition is applied:

$$\frac{\partial^2\phi}{\partial t^2}(x,y,z,t) + g\frac{\partial\phi}{\partial y_s}(x,y,z,t) = 0 \qquad \text{at} \quad y_s = -R + h \tag{10}$$

  where h and R are the blade tip immersion and blade radius, respectively (see Figure 8). y_s is the vertical ship-fixed coordinate, defined in Figure 1.

- The assumption of infinite Froude number is applied, which reduces Eqn. 10 to $\phi(x,y,z,t) = 0$ on the free surface. This implies that the "negative" image method can be used to account for the effect of the free surface. The infinite Froude number assumption is valid because surface-piercing propellers usually operate at very high speeds.

- The source and dipole strengths on the "dry" part of the blades are set equal to zero. The split-panel method is used to account for the effect of partially submerged panels. Hence, the number of unknowns is reduced to the number of fully submerged panels.
- In order to save computer time, only one iteration is performed at each timestep (i.e. the method does not iterate to determine the exact thickness of the ventilated cavity). This is assumed to be a valid approximation since the pressure is set equal to atmospheric on the ventilated portion of the blades, and the pressures on the wetted portion of the blades are not expected to be significantly affected by small differences in cavity height.

It should be noted that the program is still in the development stage for the analysis of partially submerged propellers. Thus, the effect of partially submerged panels and the hub are currently ignored.

3 Results

3.1 Fully Submerged Propellers

To validate PROPCAV, predicted force coefficients are compared with experimental measurements collected by Matsuda et al. (1994) for a supercavitating propeller. The test geometry is M.P.No.345(SRI), which is designed using SSPA charts under the following conditions: $J_s = V_s/nD = 1.10$, $\sigma_v = (P_o - P_v)/(\frac{\rho}{2}V_s^2) = 0.40$, and $K_T = T/\rho n^2 D^4 = 0.160$ (T is the propeller thrust). In the numerical evaluation, the suction side of the blade section is modified aft of the midchord to render zero thickness at the trailing edge. This treatment is valid as long as the modified blade section is inside the cavitation bubble.

The comparisons of the predicted versus measured thrust (K_T) and torque ($K_Q = Q/\rho n^2 D^5$, Q is the torque of the propeller) coefficients, as well as propeller efficiency ($\eta = \frac{K_T}{K_Q}\frac{J}{2\pi}$) are shown in Figure 3. The propeller geometry with the predicted cavities at $J_s = 1.3$ are shown in Figure 4. Also shown in Figure 4 are the predicted cavitating pressures along each radial strip at $J_s = 1.3$. It is worth noting that at this particular combination, there is substantial midchord detachment. Figure 4 indicates that the Villat-Brillouin smooth detachment criterion is satisfied since the cavity thickness is non-negative and the pressures everywhere on the wetted blade surfaces are above the vapor pressure. The comparisons shown on Figure 3 indicate that the predictions by PROPCAV agree very well with experimental data for values of $J_s \leq 1.2$. For $J_s > 1.2$, the comparisons are not as good because the cavities begin to detach aft of the midchord, where the suction side geometry was modified.

3.2 Partially Submerged Propellers

In order to validate the partially submerged propeller formulation in PROPCAV, numerical predictions for propeller model 841-B are compared with experimental measurements. A photograph of the partially-submerged propeller is shown in Figure 5. Individual dynamic blade loads were collected by Olofsson (1996) for different combinations of Froude number ($F_{nD} = V_s/\sqrt{gD}$), cavitation number (σ_v), advance coefficient (J_s), and shaft orientation. For the purpose of this comparison, the following flow conditions were selected: $J_s = 0.8$, $F_{nD} = 4.0$, $\sigma_v = 0.57$, and zero shaft yaw and inclination angle. The propeller immersion ratio, h/D, is 33 % (h is the blade tip immersion defined in Figure 8). The axial velocity distribution at the propeller plane is shown in Figure 6. At these flow conditions, the cavities are fully ventilated and the effect of Froude number and cavitation number are negligible (Olofsson (1996)).

In the numerical calculations, the blade section was modified from the original aft of the midchord in to render zero trailing edge thickness, which is shown in Figure 7. The predicted pressure contours on the wetted side of the blade are shown in Figure 8. The predicted ventilated surface sections at different timesteps are drawn in Figure 9. The predicted individual force and moment coefficients are shown in Figure 10 along with experimental data from Olofsson (1996). The solid lines and the symbols in Figure 10 represent the load coefficients predicted by PROPCAV and measured in experiments, respectively. (K_{FX}, K_{FY}, K_{FZ}, K_{MX}, K_{MY}, K_{MZ}) are the six components of the individual blade force and moment coefficients defined in the coordinate system shown in Figure 1.

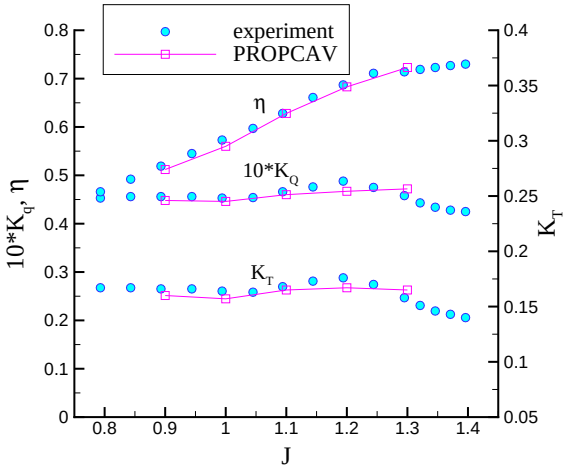

Figure 3: Comparison of the predicted and versus measured K_T, K_Q, and η for different advance coefficients. Propeller SRI. $\sigma_v = 0.4$. $\sigma_n = \sigma_v \times J_s^2$.

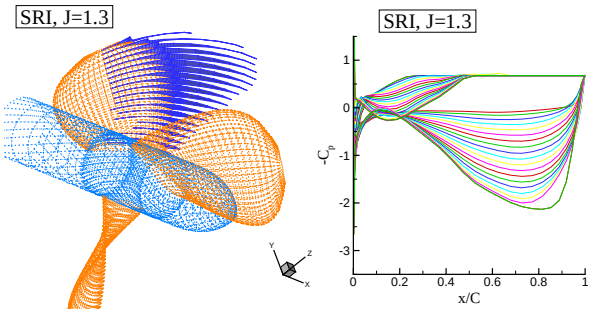

Figure 4: Geometry, cavitation pattern, and cavitating pressures for propeller SRI at $J_s = 1.3$. $\sigma_v = 0.4$. $\sigma_n = \sigma_v \times J_s^2$.

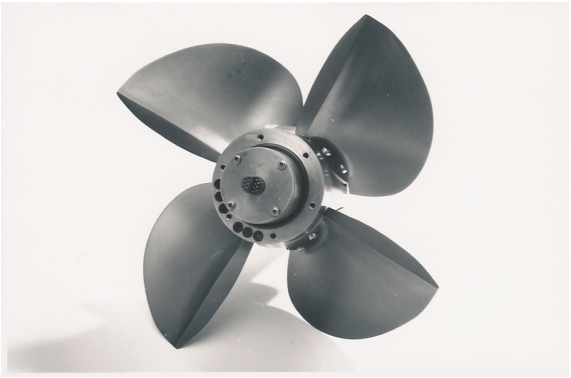

Figure 5: Photograph of propeller model 841-B (from Olofsson 1996).

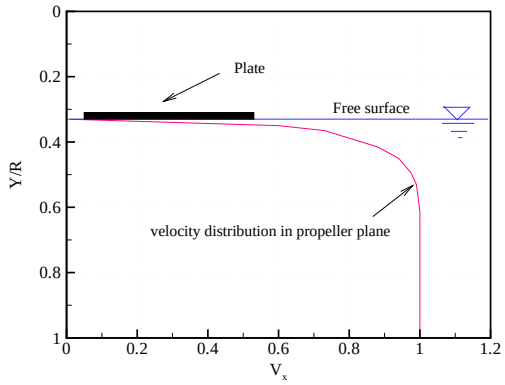

Figure 6: Axial velocity distribution at the propeller plane. Propeller model 841-B. $h/D = 0.33$.

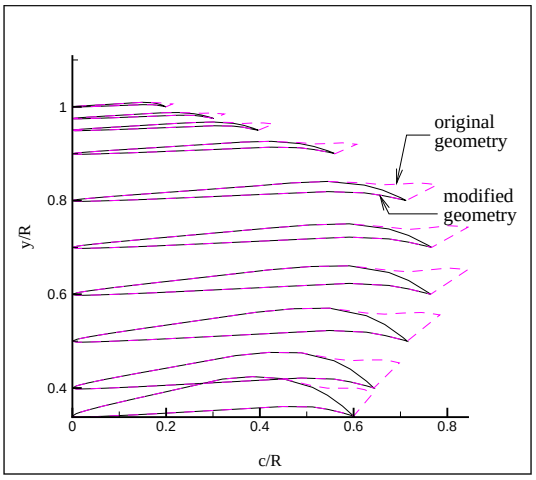

Figure 7: Original and modified (on the suction side aft the midchord) blade section geometry of propeller model 841-B.

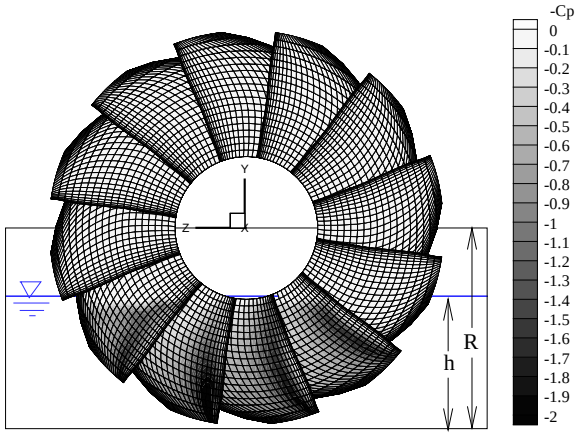

Figure 8: Pressure contours predicted by PROPCAV. Propeller model 841-B. 4 Blades. $h/D = 0.33$. $J = 0.8$. 60x20 panels. $\Delta\theta = 6^o$.

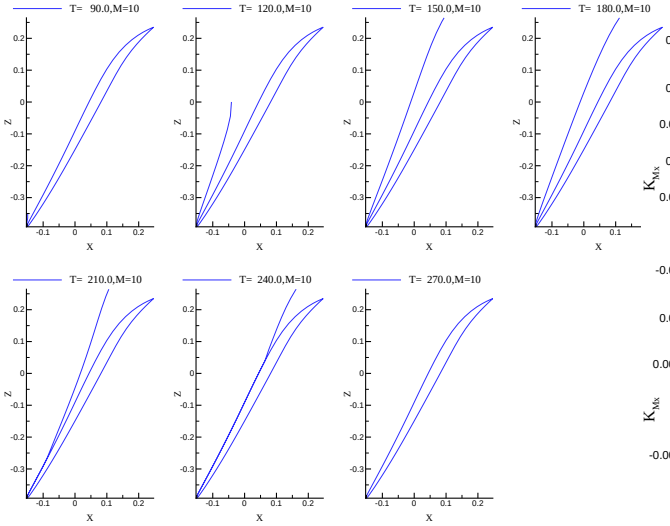

Figure 9: Ventilated surface sections at $r/R = 0.52$. Propeller model 841-B. 4 Blades. $h/D = 0.33$. $J = 0.8$. 60x20 panels. $\Delta\theta = 6^o$.

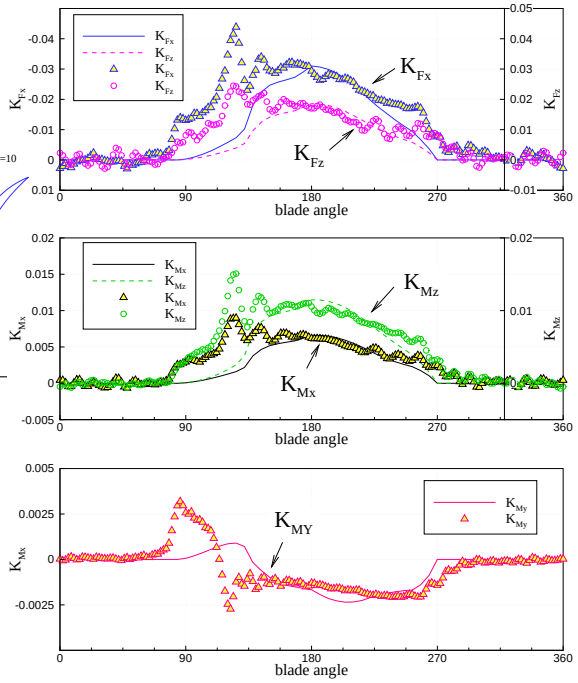

Figure 10: Comparison of the blade forces predicted by PROPCAV and by measurements from experiments. Propeller model 841-B. 4 Blades. $h/D = 0.33$. $J = 0.8$. 60x20 panels. $\Delta\theta = 6^o$.

As shown in Figure 10, the maximum force coefficients predicted by PROPCAV seemed to be in reasonable agreement with experimental measurements. However, there are discrepancies at the blade entry and exit. The major reasons for the discrepancies at the blade entry are:

1. Inadequate simulation of the blade entry phenomena. At the instant of impact, a very strong jet is developed near the blade leading edge. This results in very high slamming forces as well as increase in wetted blade area on the face side, both of which contribute significantly to the hydrodynamic loads at the entry phase. It should be noted that slamming here means impulse load with high pressure occur during impact between a blunt body and the water surface.

2. Inability of the current method to capture the effect of change in free surface elevation caused by the piercing action of the blades. The added hydrodynamic blade load is evident in Figure 10. Due to the particular design of the propeller, the actual in-water phase should range from 90^o to 270^o (Olofsson (1996)). However, the experimental data in Figure 10 indicated that the blade carries load from 70^o to 290^o.

3. Inability of the current method to model the effect of blade vibrations. Blade vibration is a resonance phenomenon which affect the blade shapes and loadings. The effect of which is evident via the "humps" (amplified fluctuations superimposed on the basic load) observed in the experimental data shown in Figure 10. It was also observed during experiments that the frequencies of these fluctuations modulate between the blade's fundamental frequency in air and in water (Olofsson (1996)).

4 Detailed 2-D Study of Free Surface Effects

In order to fully understand the slamming effect as well as the change in free surface elevation, a systematic 2-D study is being conducted. The exact free surface conditions is used and the effect of Froude number will be studied. The objective of the 2-D study is to find a simplified approach to quantify the added hydrodynamic forces due to slamming and change in free surface elevations. The progression of the proposed 2-D study is shown in Figure 11.

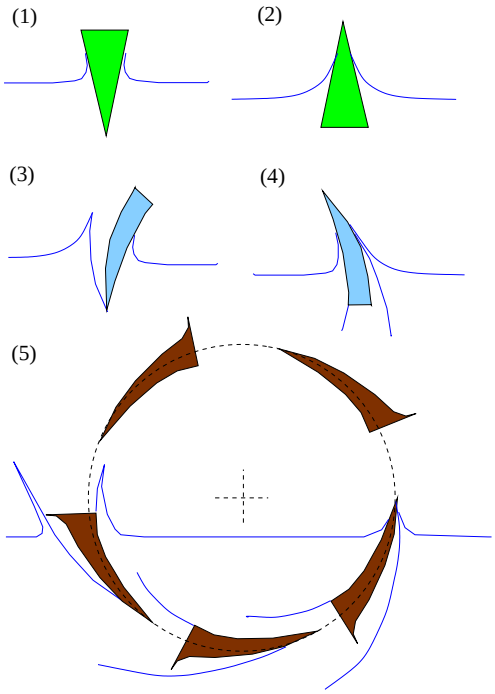

Figure 11: Proposed progression for a systematic 2-D study of the added hydrodynamic forces due to slamming and change in free surface elevation.

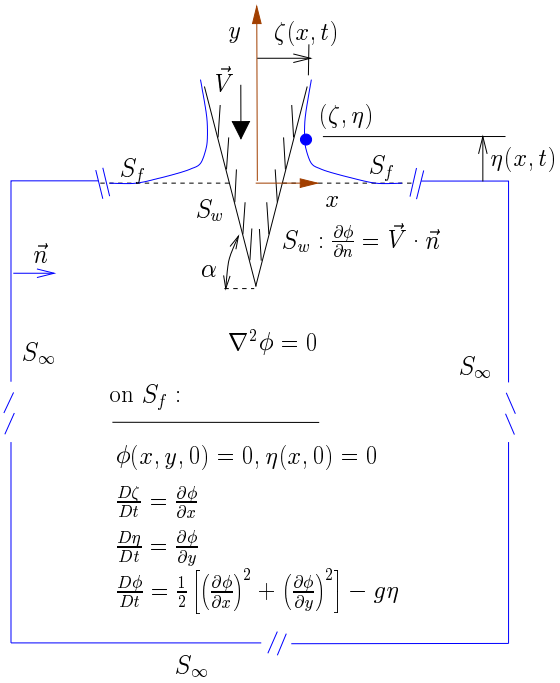

Figure 12: Definition of coordinate system and control surface for the 2-D analysis of the wedge entry problem. α is the deadrise angle.

4.1 Previous Work on the 2-D Wedge Entry Problem

The problem of a 2-D rigid wedge entering the water was first studied by Von Karman (1929) and Wagner (1932). Both assumed that the velocity field around the wetted part of the body can be approximated with the flow field around an expanding flat plate. Recently, the 2-D wedge entry problem was thoroughly investigated by Zhao and Faltinsen (1993). A non-linear boundary element method with constant source and dipole distributions was used. The jet flow occurring at the intersections between the free surface and the body was carefully considered. The method was verified by comparisons with similarity solutions and asymptotic analysis.

The first step for the proposed 2-D analysis involve analyzing the flow around a 2-D symmetric wedge entering the water. Thus, the work presented in the next sections follows similar assumptions and methodology presented by Zhao and Faltinsen (1993).

4.2 Formulation for the 2-D Wedge Entry Problem

Consider a rigid 2-D body entering into a initially calm water of an unbounded domain at a constant velocity $\vec{V}$, as shown in Figure 12. For incompressible, inviscid, and irrotational flow, the perturbation potential ϕ at any time t satisfies Laplace's equation in the fluid domain (i.e. $\nabla^2\phi(x,y,t) = 0$). Thus, the potential on the boundary, $S(t)$, of the computation domain, is represented by Green's third identity:

$$\pi\phi(x,y,t) = \int_{S(t)} \left[-\phi(\zeta,\eta,t)\frac{\partial G(\zeta,\eta,t)}{\partial n(\zeta,\eta,t)} + \frac{\partial\phi(\zeta,\eta,t)}{\partial n(\zeta,\eta,t)}G(\zeta,\eta,t)\right] dS(\zeta,\eta,t) \tag{11}$$

where $G = \ln r$, $r = \sqrt{(x-\zeta)^2 + (y-\eta)^2}$, and $S(t) = S_w(t) \cup S_f(t) \cup S_\infty$ (defined in Figure 12). $\vec{n}$ is the unit vector normal to the integration surface, which points into the fluid domain. It should be noted that for this problem, the perturbation potential (ϕ) is the same as the total potential (Φ) since the system is defined with respect to the undisturbed free surface coordinates (x,y), as shown in Figure 12.

4.2.1 Kinematic Free Surface Boundary Condition

The kinematic free surface condition requires the fluid particles to remain on the free surface:

$$\frac{\partial \eta}{\partial t} + \frac{\partial \phi}{\partial x}\frac{\partial \eta}{\partial x} = \frac{\partial \phi}{\partial y} \tag{12}$$

where $\eta(x,t)$ is the vertical displacement of fluid particles on the free surface from the undisturbed position, as shown in Figure 12.

4.2.2 Dynamic Free Surface Boundary Condition

On the exact free surface, the pressure should be constant and equal to the atmospheric pressure:

$$\frac{\partial \phi}{\partial t} + \frac{1}{2}\left[\left(\frac{\partial \phi}{\partial x}\right)^2 + \left(\frac{\partial \phi}{\partial y}\right)^2\right] + g\eta = 0 \tag{13}$$

4.2.3 Combined Free Surface Kinematic and Dynamic Boundary Condition

Equations 12 and 13 can be combined to form a system of three equations using the definition of substantial derivative, $\frac{D}{Dt} = \frac{\partial}{\partial t} + \nabla\phi \cdot \nabla$:

$$\frac{D\zeta}{Dt} = \frac{\partial \phi}{\partial x} \quad , \qquad \frac{D\eta}{Dt} = \frac{\partial \phi}{\partial y} \quad , \qquad \text{and} \qquad \frac{D\phi}{Dt} = \frac{1}{2}\left[\left(\frac{\partial \phi}{\partial x}\right)^2 + \left(\frac{\partial \phi}{\partial y}\right)^2\right] - g\eta \tag{14}$$

where $\zeta(x,t)$ is the horizontal displacement of fluid particles on the free surface from the undisturbed position, as shown in Figure 12.

4.2.4 Kinematic Body Boundary Condition

If there is a body penetrating the water surface at a constant velocity $\vec{V}$, the kinematic boundary condition requires the following condition to be satisfied on the wetted body surface:

$$\left(\nabla\phi - \vec{V}\right) \cdot \vec{n} = 0 \tag{15}$$

4.2.5 Kinematic Infinite Boundary Condition

The kinematic boundary condition at the infinite boundaries requires that the normal velocity across the boundary to be zero, i.e. $\frac{\partial \phi}{\partial n} = 0$.

4.2.6 Initial Free Surface Condition

The initial condition on the free surface are set as follows:

$$\left.\begin{array}{l} \phi(x,y,0) = 0 \\ \eta(x,0) = 0 \end{array}\right\} \quad \text{at} \quad t = 0 \tag{16}$$

4.2.7 Solution Method

At each time step, Green's formula (Eqn. 11) is solved with respect to unknowns ϕ on S_w and S_∞, and unknowns $\frac{\partial \phi}{\partial n}$ on S_f. The control surface, S, is discretized into a number of straight segments. In order to avoid singularities at intersection points, $\frac{\partial \phi}{\partial n}$ and ϕ for each panel are approximated with constant and linear strength distributions, respectively. The values of $\frac{\partial \phi}{\partial n}$ are computed at the control points, and the values of ϕ are computed at the panel end points. The generation of the jet panel follows the same method presented in Zhao and Faltinsen (1993).

The known values of $\frac{\partial \phi}{\partial n}$ on the wetted body boundary and infinite boundaries are given by the kinematic boundary conditions. The geometry and the known values of ϕ on the free surface are determine by solving

Eqn. 14 using a predictor-corrector method. The time-marching procedure on S_f is summarized below. For simplicity, the gravity term is temporarily neglected.

1. Compute the *intermediate* values of ζ, η, and ϕ at control point i on the free surface for time $n+1$:

$$\zeta_i^* = \zeta_i^n + \frac{\Delta t}{2}\left(\left.\frac{\partial\phi}{\partial x}\right|_i^n\right), \quad \eta_i^* = \eta_i^n + \frac{\Delta t}{2}\left(\left.\frac{\partial\phi}{\partial y}\right|_i^n\right), \quad \text{and} \quad \phi_i^* = \phi_i^n + \frac{\Delta t}{4}\left[\left(\left.\frac{\partial\phi}{\partial x}\right|_i^n\right)^2 + \left(\left.\frac{\partial\phi}{\partial y}\right|_i^n\right)^2\right] \tag{17}$$

2. Solve Green's formula, Eqn. 11, to obtain values of ϕ^* and $\frac{\partial\phi}{\partial n}^*$ everywhere for the intermediate step.

3. Compute the intermediate velocities, $\frac{\partial\phi}{\partial x}^*$ and $\frac{\partial\phi}{\partial y}^*$, at the control points:

$$\frac{\partial\phi}{\partial x} = \frac{\partial\phi}{\partial s}s_x + \frac{\partial\phi}{\partial n}n_x \quad , \qquad \frac{\partial\phi}{\partial y} = \frac{\partial\phi}{\partial s}s_y + \frac{\partial\phi}{\partial n}n_y \tag{18}$$

   (s_x,s_y) are the x and y components of the tangential unit vector, respectively. (n_x,n_y) are the x and y components of the normal unit vector, respectively.

4. Compute the *corrected* values of ζ, η, and ϕ on the free surface for time $n+1$:

$$\zeta_i^{n+1} = \zeta_i^n + \Delta t\left(\left.\frac{\partial\phi}{\partial x}\right|_i^*\right), \quad \eta_i^{n+1} = \eta_i^n + \Delta t\left(\left.\frac{\partial\phi}{\partial y}\right|_i^*\right), \quad \text{and} \quad \phi_i^{n+1} = \phi_i^n + \frac{\Delta t}{2}\left[\left(\left.\frac{\partial\phi}{\partial x}\right|_i^*\right)^2 + \left(\left.\frac{\partial\phi}{\partial y}\right|_i^*\right)^2\right] \tag{19}$$

5. Solve Green's formula, Eqn. 11, to obtain values of ϕ^{n+1} and $\frac{\partial\phi}{\partial n}^{n+1}$ everywhere for the corrector step.

6. Compute the corrected velocities, $\frac{\partial\phi}{\partial x}^{n+1}$ and $\frac{\partial\phi}{\partial y}^{n+1}$, at the control points using Eqn. 18.

Once ϕ and $\frac{\partial\phi}{\partial n}$ are known everywhere for time step $n+1$, the pressures on S_w are computed at time step $n+\frac{1}{2}$ as follows:

$$\left.\frac{p}{\rho}\right|_i^{n+\frac{1}{2}} = -\left.\frac{\partial\phi}{\partial t}\right|_i^{n+\frac{1}{2}} - \frac{1}{2}\left[\left(\left.\frac{\partial\phi}{\partial x}\right|_i^{n+\frac{1}{2}}\right)^2 + \left(\left.\frac{\partial\phi}{\partial y}\right|_i^{n+\frac{1}{2}}\right)^2\right] \tag{20}$$

where

$$\left.\frac{\partial\phi}{\partial x}\right|_i^{n+\frac{1}{2}} = \frac{1}{2}\left[\left.\frac{\partial\phi}{\partial x}\right|_i^n + \left.\frac{\partial\phi}{\partial x}\right|_i^{n+1}\right] \qquad \left.\frac{\partial\phi}{\partial y}\right|_i^{n+\frac{1}{2}} = \frac{1}{2}\left[\left.\frac{\partial\phi}{\partial y}\right|_i^n + \left.\frac{\partial\phi}{\partial y}\right|_i^{n+1}\right]$$

$$\left.\frac{\partial\phi}{\partial t}\right|_i^{n+\frac{1}{2}} = \frac{\phi_i^{n+1} - \phi_i^n}{\Delta t} - \left[\left(\left.\frac{\partial\phi}{\partial x}\right|_i^{n+\frac{1}{2}}\right)^2 + \left(\left.\frac{\partial\phi}{\partial y}\right|_i^{n+\frac{1}{2}}\right)^2\right]$$

Following the pressure computation, all the nodes are redistributed so that high density of panels are maintained in areas of high curvature on S_f and S_B, as well as in areas around the jet. The values ϕ and $\frac{\partial\phi}{\partial n}$ are then interpolated for the new particle positions prior to the computations for the next time step.

4.3 Results for the 2-D Wedge Entry Problem

The predicted free surface elevations and pressures on the body for a wedge entering the water at α (dead rise angle) = 81^o are shown in Figure 13. The velocity flow field near the jet is shown in Figure 14. The predicted results compare well with the those presented in Zhao and Faltinsen (1993).

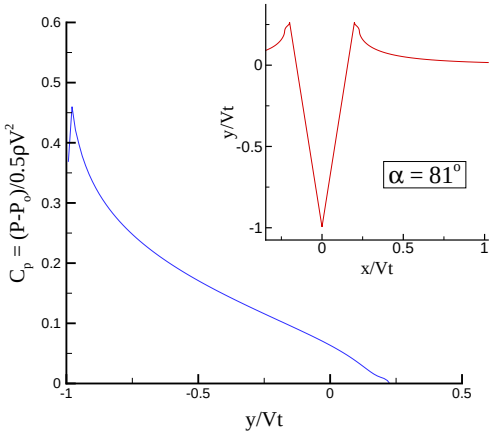

Figure 13: Predicted free surface elevations and pressures on the wedge. $\alpha = 81^o$.

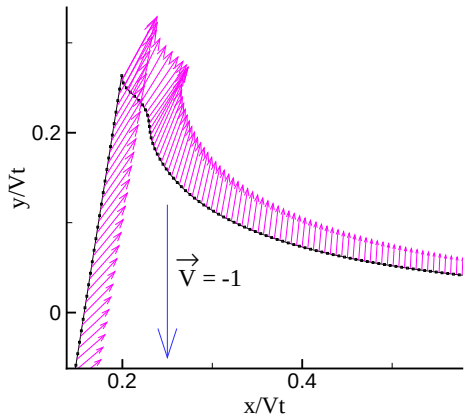

Figure 14: Predicted velocity flow fields around the jet. $\alpha = 81^o$. The flow is defined with respect to the coordinate system (x, y) fixed on the undisturbed free surface.

5 Conclusions

A 3-D boundary element method, PROPCAV, for the analysis of fully submerged and partially submerged propellers was described. An overview of the formulation and solution method was presented. The numerical predictions by PROPCAV for a fully submerged supercavitating propeller and a surface-piercing propeller were presented along with experimental measurements. The modeling of the jet flow around a 2-D body entering the free surface was provided.

Current efforts in PROPCAV include the following:

- A systematic 2-D study of the added hydrodynamic blade loads due to slamming and change in free surface elevation at the blade entry and exit.
- Extension of the 2-D non-linear free surface algorithm to 3-D (i.e. incorporate it into PROPCAV).
- Validations with experimental measurements, and studies of numerical sensitivity to the space and time discretization.
- Coupling of the hydrodynamics with a structural analysis model to include the effect of blade vibrations.

Acknowledgment

Support for this research was provided by Phases II and III of the "Consortium on Cavitation Performance of High Speed Propulsors" with the following members: AB Volvo-Penta, American Bureau of Shipping, Office of Naval Research and David Taylor Model Basin, Daewoo Shipbuilding & Heavy Machinery, El Pardo Model Basin, Hyundai Maritime Research Institute, John Crane-Lips Norway AS, Kamewa AB, Michigan Wheel, Rolla SP Propellers SA, Ulstein Propeller AS, and VA Tech Escher Wyss GMBH. The authors wish to thank Dr. Niclas Olofsson for providing the experimental data.

References

Choi, J. (2000). *Vortical Inflow – Propeller Interaction Using Unsteady Three-Dimensional Euler Solver*. PhD thesis, Department of Civil Engineering, The University of Texas at Austin.

Fine, N. E. (October, 1992). *Nonlinear Analysis of Cavitating Propellers in Nonuniform Flow*. PhD thesis, Department of Ocean Engineering, MIT.

Furuya, O. (1984). A performance prediction theory for partially submerged ventilated propellers. In *Fifteenth Symposium on Naval Hydrodynamics*, Hamburg, Germany.

Kinnas, S., Choi, J., Lee, H., and Young, J. (2000). Numerical cavitation tunnel. In *NCT50, International Conference on Propeller Cavitation*, Newcastle upon Tyne, England.

Kinnas, S. and Fine, N. (1991). Non-Linear Analysis of the Flow Around Partially or Super-Cavitating Hydrofoils by a Potential Based Panel Method. In *Boundary Integral Methods-Theory and Applications, Proceedings of the IABEM-90 Symposium, Rome, Italy, October 15-19, 1990*, pages 289–300, Heidelberg. Springer-Verlag.

Kinnas, S. and Fine, N. (1992). A nonlinear boundary element method for the analysis of unsteady propeller sheet cavitation. In *Nineteenth Symposium on Naval Hydrodynamics*, pages 717–737, Seoul, Korea.

Kinnas, S. and Fine, N. (1993). A numerical nonlinear analysis of the flow around two- and three-dimensional partially cavitating hydrofoils. *Journal of Fluid Mechanics*, 254:151–181.

Kudo, T. and Kinnas, S. (1995). Application of vortex/source lattice method on supercavitating propellers. In *24th American Towing Tank Conference*, College Station, TX.

Kudo, T. and Ukon, Y. (1994). Calculation of supercavitating propeller performance using a vortex-lattice method. In *Second International Symposium on Cavitation*, pages 403–408, Tokyo, Japan.

Matsuda, N., Kurobe, Y., Ukon, Y., and Kudo, T. (1994). Experimental investigation into the performance of supercavitating propellers. *Papers of Ship Research Institute*, 31(5).

Morgan, W. (1966). The testing of hydrofoils for fully-cavitating or ventilated operations. In *The 11th ITTC*, Tokyo, Japan.

Mueller, A. (1998). Development of face and mid-chord cavitation models for the prediction of unsteady cavitation on a propeller. Master's thesis, UT Austin, Dept. of Civil Engineering.

Mueller, A. and Kinnas, S. (1999). Propeller sheet cavitation predictions using a panel method. *Journal of Fluids Engineering*, 121:282–288.

Oberembt, H. (1968). Zur bestimmung der instationären flügelkräfte bei einem propeller mit aus dem wasser herausschlagenden flügeln. Technical report, Inst. für Schiffau der Universität Hamburg, Bericht Nr. 247.

Olofsson, N. (1996). *Force and Flow Characteristics of a Partially Submerged Propeller*. PhD thesis, Department of Naval Architecture and Ocean Engineering, Chalmers University of Technology, Göteborg, Sweden.

Savineau, C. and Kinnas, S. (1995). A numerical formulation applicable to surface piercing hydrofoils and propellers. In *24th American Towing Tank Conference*, Texas A&M University, College Station, TX.

Scherer, J. (1977). Partially submerged and supercavitating propellers. In *The 18th ATTC*, Annapolis.

Shen, Y. (1975). General scaling problems on fully cavitating and ventilated flows. In *The 17th ATTC*, Pasadena.

Suhrbier, K. and Lecoffre, Y. (1986). Investigation of the influences of test techniques, water speed and nucliei seeding on the characteristics of a high speed model propeller in a cavitation tunnel and correlation with full scale measurements. In *International Symposium on Cavitation*, Sendai, Japan.

Von Karman, T. (1929). The impact of seaplane floats during landing. Technical report, NACA TN321.

Wagner, H. (1932). Über stoss- und gleitvorgänge an der oberflänche von flüssigkeiten. *Z. Angew. Math. Mech.*, 12(4):pp. 192–215.

Young, Y. and Kinnas, S. (2001). A BEM for the prediction of unsteady midchord face and/or back propeller cavitation. *Journal of Fluids Engineering*.

Zhao, R. and Faltinsen (1993). Water entry of two-dimensional bodies. *Journal of Fluid Mechanics*, 246:pp. 593–612.